



# Optimization and Experimental Validation of a Robust S-Duct Geometry with Boundary-Layer Ingestion

Inès Chikhaoui\*

*Institute for Aerospace Studies, University of Toronto, Toronto, Ontario, M3H 5T6, Canada*

Catherine Clark<sup>†</sup>, Faezeh Rasimarzabadi<sup>‡</sup> and Hugo Breton<sup>§</sup>

*National Research Council of Canada, Ottawa, Ontario, K1A 0R6, Canada*

Hamza abo el Ella<sup>¶</sup>

*Mechanical and Aerospace Engineering, Faculty of Engineering and Design, Carleton University, Ottawa, Ontario, K1S 5B6, Canada*

David W. Zingg<sup>||</sup>

*Institute for Aerospace Studies, University of Toronto, Toronto, Ontario, M3H 5T6, Canada*

An S-duct intake for a boundary-layer ingesting engine has been designed using a gradient-based aerodynamic shape optimization framework based on the Reynolds-averaged Navier–Stokes equations. The optimization minimizes a composite objective function that combines total pressure loss and circumferential flow distortion at the fan face. To improve robustness across varying operating conditions, a multi-point optimization was conducted over a range of incoming boundary-layer thicknesses between 20 and 40% of the inlet height. The optimized geometry was fabricated and tested experimentally using a custom-built test rig. Experimental measurements of pressure loss, circumferential distortion, and swirl at the fan face are compared to numerical predictions, showing good agreement. Low circumferential flow distortion was observed experimentally with the multi-point-optimized geometry, confirming the effectiveness of the optimization framework.

## Nomenclature

$A$	area
$D$	circumferential distortion
$J$	optimization parameter
$P_T$	total pressure
$PR$	pressure recovery
$S$	swirl
$U$	velocity
$x$	streamwise position
$\theta$	angular position
$\alpha_s$	flow angle

\*PhD Candidate, ines.chikhaoui@mail.utoronto.ca

<sup>†</sup>Senior Research Officer, Aerodynamics Laboratory

<sup>‡</sup>Senior Research Officer, Power and Propulsion Laboratory

<sup>§</sup>Senior Mechanical Designer, Design and Fabrication Services

<sup>¶</sup>Associate Professor, Hamzaella@cunet.carleton.ca

<sup>||</sup>Professor, University of Toronto Distinguished Professor of Computational Aerodynamics and Sustainable Aviation and Associate Fellow AIAA, david.zingg@utoronto.ca

## I. Introduction

Turbojet propulsion began with Frank Whittle's design of the first turbojet engine in 1930, leading to the first flight of a turbojet-powered aircraft in 1939. Over time, the configuration and performance of these engines evolved considerably, progressing to the adoption of turbofan engines designed for improved fuel efficiency through higher bypass ratios. While turbofans remain the backbone of contemporary commercial aviation, increasing propulsive efficiency by ingesting larger mass flows has necessitated larger fan diameters, leading to greater structural weight and aerodynamic drag. Despite continuous improvements in engine technology, the pace of efficiency gains has slowed in recent decades as the design matured. Concurrently, the steady rise in global air traffic has put pressure on the aviation sector to address its environmental footprint. As a result, regulatory bodies have outlined ambitious targets aimed at reducing fuel consumption to reach net zero carbon emissions by 2050. Advanced aircraft technologies are expected to play a significant role in this transition.

One promising advanced propulsion concept is boundary-layer ingestion (BLI), which offers the potential to significantly enhance propulsive efficiency by rethinking the integration of propulsion and airframe design. This concept originates from the marine sector, where it is commonly applied to submarines and ships [1, 2]. BLI can result in less power being required to produce a given propulsive thrust force, as analyzed by Smith [3]. It is now receiving much attention as a way to improve fuel efficiency in concept studies for advanced aircraft [4–7]. Current-generation aircraft commonly feature engine placements away from the nearest aircraft surface to ensure ingestion of uniform freestream air. In contrast, boundary-layer-ingesting engines are usually positioned such that they ingest the boundary-layer on the wing or fuselage. This allows for a reduction in the momentum deficit of the aircraft wake, lowering the propulsion work required to overcome total aircraft drag. Depending on the level of ingestion and the configuration, some studies have reported a potential aerodynamic benefit of approximately 10% [7], which corresponds to the savings in mechanical flow power required in a BLI configuration relative to non-BLI.

Many BLI configurations have been explored, including NASA's STARC-ABL single-aisle commercial aircraft concept which explores electrified aircraft propulsion technologies coupled with an aft-mounted BLI engine running on energy from two under-wing turbofan engines. This concept has the potential to reduce fuel burn by 7% to 12% compared to current regional jets operating with the same range, speed, and airport infrastructure [8]. Another concept investigated is MIT's D8 Double-Bubble which features twin cylindrical fuselages paired with BLI in a Boeing 737 class aircraft. Wind-tunnel tests and computational assessments demonstrate a potential aerodynamic benefit of about 8% [7].

These advantages, however, come with new design complexities. The ingested flow is strongly non-uniform, creating inlet distortions that can reduce fan performance and structural integrity. Fan-face radial total pressure distortion describes variations in total pressure from the hub (or center of the aerodynamic interface plane) toward the tip of the fan annulus (or walls of the S-duct). Circumferential total pressure distortion, on the other hand, refers to variations in total pressure around the tangential direction. It typically manifests as localized sectors of low and high total pressure caused by the intake geometry, non-uniform incoming flow, and boundary-layer development inside the duct, among other factors. Circumferential distortion is often more critical, as it introduces non-uniform loading on the fan blades, potentially triggering stall, surge, or fatigue. When designing a BLI system, it is crucial to develop an intake that minimizes circumferential distortion at the fan face and a fan that can operate reliably under the remaining distortion levels.

S-duct intakes are often employed in BLI architectures where embedded engine installation is required, as they enable compact airframe integration [9]. However, the curvature of S-ducts leads to complex secondary flow structures, flow separation, and total pressure distortion at the fan face. To mitigate these effects, several design strategies have been explored, including boundary layer suction [10], the use of flow control [11], as well as high-fidelity optimization approaches [12–17]. Papadopoulos et al. [18] numerically investigated the impact of S-duct geometry variations on aerodynamic efficiency. The study found that reducing the axial length of the duct increased flow separation after the first bend, leading to higher losses, whereas long ducts caused greater pressure losses but achieved a more uniform total pressure distribution. The adoption of Gerlach-shaped cross-sectional profiles in the S-duct design yielded a low level of pressure loss. Koo et al. [15] developed an aerodynamic shape optimization methodology based on the Reynolds-averaged Navier-Stokes equations aimed at improving the aerodynamic performance of a fixed rectangular S-duct intake with BLI, specifically designed for a high-subsonic unmanned aerial vehicle. The primary objectives of the study were to enhance total pressure recovery while minimizing outlet circumferential distortion. One outcome of the optimization was the increased swirl observed in the resulting duct designs compared to the baseline configuration. Chiang, Koo, and Zingg [16] subsequently conducted a comprehensive study on the aerodynamic shape optimization of an S-duct intake for a BLI engine utilizing the same optimization framework, this time considering two composite

objective functions. The first combines total pressure recovery, distortion and swirl at the fan interface plane, while the second involves pressure recovery, fan blade load variation, and fan blade incidence variation. They achieved a simultaneous improvement in all objectives contained in the composite objective functions through subtle geometric modifications. In a later study, Clark et al. [17] focused on a geometry optimization and experimental validation of an S-duct with BLI. An S-duct intake for a BLI engine was designed to minimize a combination of total pressure loss and circumferential flow distortion at the outlet through the optimization methodology used in [15, 16]. The experimental data showed reasonable agreement with the numerical predictions.

The objective of this paper is to optimize and experimentally confirm the performance of a boundary-layer ingesting S-shaped intake designed to minimize circumferential flow distortion and total pressure losses under varying inlet conditions. The geometry is generated using multi-point optimization considering a range of incoming boundary-layer thicknesses in order to design a duct that is less sensitive to inevitable differences between simulation and experiment in order to achieve better agreement.

The paper is organized as follows. Section II describes the overall methodology, beginning with a description of the aerodynamic shape optimization framework and optimization problem formulation, followed by an overview of the experimental setup. Section III discusses the results of the optimization study. In Section IV, the numerical predictions are compared against experimental data to assess the performance and accuracy of the optimized geometry. Finally, Section V summarizes the main findings and offers concluding remarks.

## II. Methodology

### A. Aerodynamic Shape Optimization Methodology

Aerodynamic shape optimization is performed using *Jetstream*, a software suite developed at the University of Toronto Institute for Aerospace Studies [19–22]. *Jetstream* integrates several key components: a geometry parameterization and mesh deformation framework, free-form deformation (FFD) geometry control, a parallel flow solver for the Reynolds-averaged Navier–Stokes (RANS) equations, and the gradient-based nonlinear optimization algorithm SNOPT with gradients computed via the discrete adjoint method.

The optimization process begins by discretizing the flow domain into a multi-block structured mesh. To enable geometry control and mesh deformation, the geometry is parameterized using B-spline surface patches, whose control points are manipulated through a free-form deformation (FFD) volume. Further details are provided in Refs. [19, 20].

The flow field is computed using a parallel, multi-block finite-difference RANS solver [21]. Spatial discretization is performed using second-order summation-by-parts operators, while boundary conditions and block interfaces are enforced using simultaneous approximation terms. The flow solution proceeds in two stages: an initial approximate-Newton phase provides globalization, followed by an inexact-Newton phase for fast and deep convergence to steady state. The linear systems arising in each Newton step are solved using the Generalized Minimum Residual method with preconditioning based on an approximate Schur complement. The solver incorporates the Spalart–Allmaras one-equation turbulence model with SA-neg and QCR modifications and has been verified through participation in the Fifth AIAA Drag Prediction Workshop [21]. The suitability of the Spalart–Allmaras model for internal flows was assessed by comparing the surface pressure distribution over the S-duct to experimental data and CFD results from Asghar et al. [23], showing good agreement, consistent with a prior assessment by Yaras and Grosvenor [24].

Gradients are computed by solving flow and mesh adjoint problems [22] and are then passed to SNOPT (Sparse Nonlinear OPTimizer) [25], a sequential quadratic programming (SQP) algorithm designed for large-scale, constrained optimization. SNOPT updates the design variables, the mesh deformation framework updates the grid for the next iteration, and the process repeats until convergence.

### B. Experimental Methodology

A schematic of the test rig is shown in Figures 1, 2, and 3. Air is drawn into the test rig through a bellmouth inlet positioned upstream of the S-duct. Flow is supplied using a high-capacity compressor, while a gate valve downstream is used to control the test section pressure, enabling simulation of altitude effects by reducing the total pressure. A bypass region, illustrated in Figure 2, was installed around the S-duct inlet to ensure that the duct ingests only the boundary layer from the boundary-layer generator, while avoiding ingestion of the boundary layers developing along the sidewalls and ceiling.

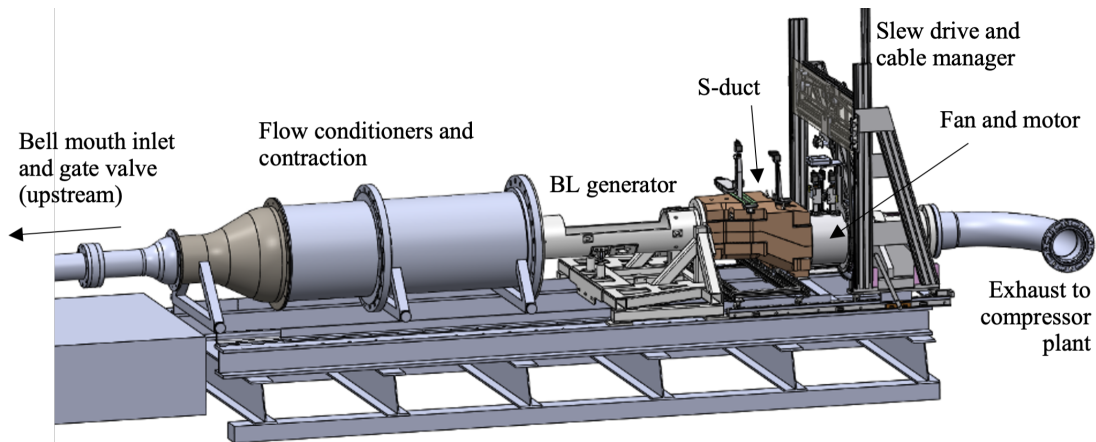


**Fig. 1 Test rig schematic**

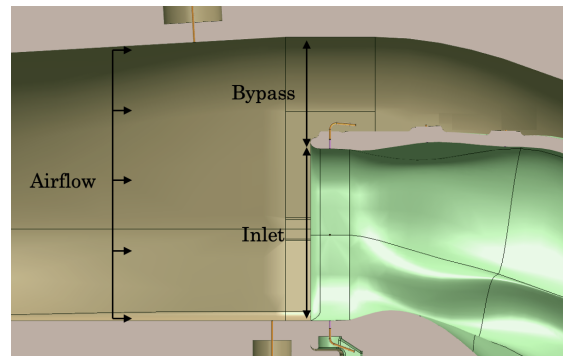


**Fig. 2 Bypass flow path surrounding the S-duct inlet**

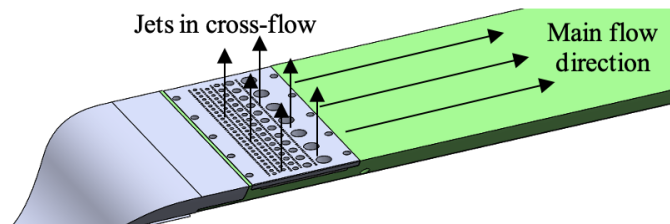


**Fig. 3 Boundary-layer generator design.**

The rig has been calibrated to deliver accurate freestream total and static pressure conditions upstream of the inlet. The boundary-layer thickness at the S-duct inlet is controlled by adjusting the mass flow ratio between the boundary-layer generator and the total system mass flow. The boundary-layer generator thickens the incoming boundary-layer to replicate conditions representative of BLI inlets on a blended-wing-body configuration. It introduces high-pressure air through a perforated plate, located flush with the lower surface of the inlet, to simulate flow over a large, uniform forebody. The design of the perforated plate primarily follows the approaches presented in [26, 27]. The plate is intended to increase the boundary-layer thickness while preserving a naturally developed turbulent boundary-layer velocity profile and corresponding turbulence intensity levels. Since larger-diameter jets penetrate deeper into the free stream and generate turbulence farther from the wall, a combination of different jet diameters is employed to achieve the desired turbulence distribution within the boundary layer. Additional details on the boundary-layer control system are shown in Figure 3 and further information on the test rig architecture and the boundary-layer generator can be found in [17].

### III. Optimization Results

#### A. Optimization Problem Formulation

The objective function used is defined as

$$J = \alpha\beta \frac{p_{t,\text{out},0}}{p_{t,\text{out}}} + (1 - \beta) \frac{D}{D_0} + \beta(1 - \alpha) \frac{S}{S_0}, \quad (1)$$

where  $p_{t,\text{out},0}$ ,  $D_0$ , and  $S_0$  denote the outlet total pressure, circumferential distortion of total pressure, and swirl, respectively, for the initial geometry. The scalar weights  $\alpha$  and  $\beta$  control the trade-off between three competing design objectives: minimization of total pressure losses, fan-face circumferential distortion, and swirl.

The first term in Eq. (1) reflects the total pressure recovery obtained by comparing the outlet total pressure at a given design iteration to that of the baseline geometry. It is defined as

$$PR = \frac{p_{t,\text{out}}}{p_{t,\text{in}}}, \quad (2)$$

where  $p_{t,\text{in}}$  and  $p_{t,\text{out}}$  are the area-averaged total pressures at the inlet and outlet planes, respectively.

The second term captures the level of circumferential total pressure distortion at the fan-face plane, which is discretized into  $m$  concentric rings, each containing  $n_j$  elements. The distortion metric  $D$  is computed as the area-weighted sum of squared deviations of local total pressure from the average total pressure within each ring:

$$D = \sum_{j=1}^m \sum_{i=1}^{n_j} \frac{(p_{t,i,j} - p_{t,\text{avg},j})^2 dA_{i,j}}{A_j}, \quad (3)$$

where  $p_{t,i,j}$  is the total pressure at element  $i$ ,  $p_{t,\text{avg},j}$  is the ring-averaged total pressure for ring  $j$ ,  $dA_{i,j}$  is the area of element  $i$ , and  $A_j$  is the total area of ring  $j$ . Non-dimensionalization is performed following the methodology of [28], with the outlet diameter used as the reference length and the upstream conditions as the reference conditions.

The final term in the objective function measures the swirl at the outlet, defined as the area-weighted average of the swirl angle magnitudes over all elements in the outlet plane:

$$S = \frac{1}{A_{\text{rings}}} \sum_{j=1}^m \sum_{i=1}^{n_j} |\alpha_s| dA_{i,j}, \quad (4)$$

where the local swirl angle  $\alpha_s$  is defined as

$$\alpha_s = \arctan\left(\frac{U_\theta}{U_x}\right), \quad (5)$$

with  $U_\theta$  and  $U_x$  representing the circumferential and axial components of the velocity vector, respectively.

To optimize the S-duct over a range of thicknesses of the ingested boundary layer, a multi-point objective function is minimized:

$$J_{\text{mp}} = 0.25J_{20\%} + 0.5J_{30\%} + 0.25J_{40\%}, \quad (6)$$

where the subscripts indicate the boundary-layer height, expressed as a percentage of the inlet height. The 30% case is considered the nominal operating condition. Conditions with higher and lower incoming boundary-layer thickness are added with a weight of 25% each.

The S-duct has a fixed length-to-offset ratio of 2.88, a length-to-diameter ratio of 1.87, a diffusion ratio of 1.3373, and a diameter of 179.1 mm. The outlet was maintained as a fixed circular geometry capable of containing a rotor. The baseline duct was taken as a simple blend between the rectangular inlet and circular outlet, adapted from Asghar [23]'s baseline geometry, with length, offset and diffusion ratio changed to the values given above. The optimization was performed at a target freestream inlet Mach number of 0.16, a Reynolds number based on the outlet diameter of 411,700, and a simulated altitude with an inlet total pressure specified at 64 kPa as imposed by the experimental facility. For the numerical simulation, total pressure was specified at the inlet, and the outlet static pressure is determined to achieve the desired Mach number at the inlet outside the incoming boundary-layer. In order to simulate boundary-layer ingestion, the turbulent flow over a two-dimensional flat plate is first solved for the desired boundary-layer height and the total pressure and turbulent viscosity profiles are extracted and applied at the inlet of the S-duct.

**Table 1 Distortion, pressure recovery, and swirl values for single-point optimized ducts with two sets of relative weights and two levels of grid refinement**

Objective	Coarse grid (1.2 million nodes)			Fine grid (4.7 million nodes)		
	Baseline	$(\alpha = 1, \beta = 0.2)$	$(\alpha = 1, \beta = 0.8)$	Baseline	$(\alpha = 1, \beta = 0.2)$	$(\alpha = 1, \beta = 0.8)$
$PR$	0.99412	0.99591	0.99594	0.99436	0.99589	0.99608
$D \times 10^5$	41.9	1.36	0.670	41.6	1.44	1.23
$S$	0.162	0.125	0.126	0.163	0.133	0.120

**Table 2 Performance of the intake obtained from a single-point optimization with a 30% boundary-layer thickness analysed with 20%, 30%, and 40% incoming boundary-layer thicknesses**

Objective	Single-point (20%)	Single-point (30%)	Single-point (40%)
$PR$	0.99780	0.99773	0.99478
$D \times 10^5$	1.50	1.19	1.33
$S$	0.122	0.121	0.119

## B. Single-point Optimization

A parametric study was conducted to evaluate the influence of the objective function weights,  $\alpha$  and  $\beta$ , on the optimization outcome. The goal was to identify weight combinations that minimize outlet swirl and total pressure distortion, while preserving or enhancing total pressure recovery. The weight  $\beta$  was varied over the discrete set  $\{0, 0.2, 0.4, 0.6, 0.8, 1.0\}$  for two fixed values of  $\alpha$ :  $\alpha = 1.0$  and  $\alpha = 0.6$ . The baseline geometry is an unoptimized initial duct geometry adapted from Asghar et al.[23]. Reducing  $\alpha$  from 1.0 to 0.6 led to a slight improvement in swirl mitigation, with a reduction factor of 1.9 relative to the baseline, compared to 1.3 for the  $\alpha = 1.0$  case. This gain, however, came at the expense of significantly degraded distortion performance, with only a 6-fold improvement relative to baseline, versus a 30-fold improvement when  $\alpha = 1.0$ . Based on this trade-off,  $\alpha = 1.0$  was adopted for all subsequent optimizations, thereby eliminating swirl from the objective function. Table 1 summarizes the pressure recovery, distortion, and swirl for the baseline geometry and for single-point optimized geometries evaluated under two combinations of  $\alpha$  and  $\beta$  and two levels of grid refinement with a 30% incoming boundary layer height. For a fixed  $\alpha$ , decreasing  $\beta$  is generally expected to enhance distortion reduction by increasing the emphasis on the distortion term in the objective function. Surprisingly, the configuration with  $\beta = 0.8$  achieved lower distortion levels than the  $\beta = 0.2$  case on both coarse and fine meshes. This is indicative of multimodality, which has been identified previously in S-duct optimization [16]. The geometry obtained with  $\beta = 0.2$  is a local minimum. In order to avoid converging to a similar local minimum, the geometry corresponding to  $\alpha = 1.0$  and  $\beta = 0.8$  was used as the initial geometry for all optimized ducts discussed below. Furthermore, it was observed that the coarse mesh failed to capture certain flow features, leading to an underestimation of the total pressure distortion at the outlet. Therefore, the fine mesh is used for all results discussed below.

A single-point optimization was performed with  $\alpha = 1$  and  $\beta = 0.2$  at the 30% incoming boundary layer condition, initialized using the optimized duct geometry obtained for the relative weights  $\alpha = 1$  and  $\beta = 0.8$ . The resulting total pressure recovery, outlet circumferential total pressure distortion, and swirl levels for different incoming boundary layer thicknesses are summarized in Table 2. In comparison with the  $\alpha = 1, \beta = 0.2$  result in Table 1, the duct obtained with a different initial geometry performs better, confirming multimodality. For example, circumferential distortion was reduced from  $1.44 \times 10^{-5}$  to  $1.19 \times 10^{-5}$ .

## C. Multi-point Optimization

### 1. Converged Optimization

Results from the fully-converged multi-point optimization are presented to demonstrate the effectiveness of the proposed strategy in mitigating fan-face flow distortion. To assess the benefits of this approach, an off-design analysis was conducted using the duct optimized for a 30% boundary-layer thickness evaluated at different inlet conditions. The corresponding objective function values for the single-point, off-design analyses, and multi-point are summarized in

**Table 3 Fully-converged multi-point optimized performance values of pressure recovery, distortion, and swirl for a fine grid resolution**

Objective	Multi-point (20%)	Multi-point (30%)	Multi-point (40%)
$PR$	0.99777	0.99771	0.99767
$D \times 10^5$	1.47	1.25	1.17
$S$	0.124	0.122	0.121

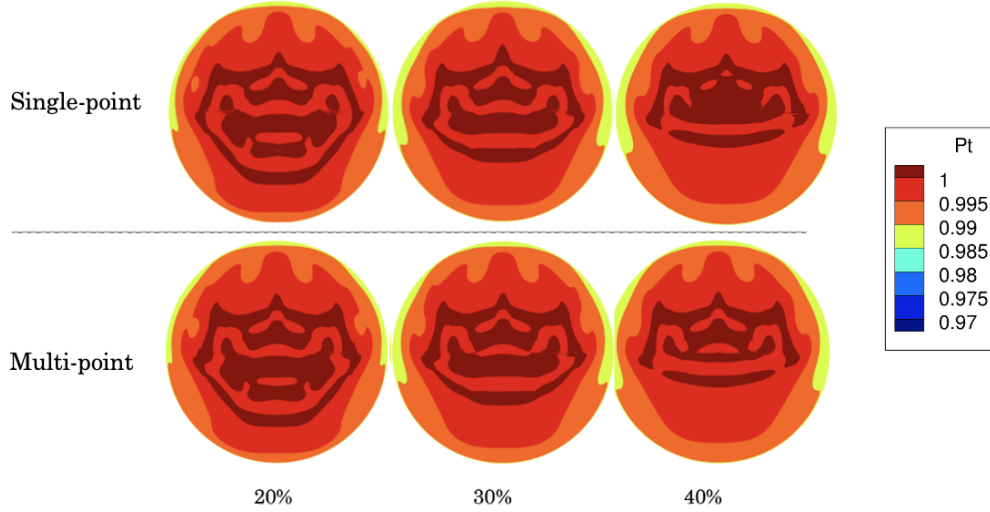


**Fig. 4 Outlet total pressure contours of the converged multi-point and single-point optimized S-duct intakes at various incoming boundary-layer heights**

Tables 2 and 3. The multi-point optimized duct demonstrates reduced sensitivity to variations in inlet boundary-layer thickness, maintaining superior overall performance across a range of inlet conditions. At the 30% boundary-layer thickness, the multi-point-optimized duct shows an increase in circumferential distortion relative to the single-point-optimized duct from  $1.19 \times 10^{-5}$  to  $1.25 \times 10^{-5}$ . At the 20% boundary-layer thickness the distortion is reduced from  $1.50 \times 10^{-5}$  to  $1.47 \times 10^{-5}$  with a large improvement seen for the 40% boundary-layer thickness, where it is reduced from  $1.33 \times 10^{-5}$  to  $1.17 \times 10^{-5}$ . If improved performance were desired at the main operating condition, this could be achieved by increasing its weight in the composite objective function. The outlet total pressure contours for both the single-point and multi-point optimized ducts are presented in Figure 4.

The first row of Figure 5 shows the baseline unoptimized duct and the multi-point optimized duct. Cross-sectional views comparing the two ducts are shown in the second row. Notable geometric changes appear in the second and third cross-sections from the inlet. Further downstream, the differences between the baseline and optimized cross-sections become less pronounced, as geometric modifications near the outlet are restricted to preserve a smooth transition into the fixed downstream section. The third row of Figure 5 presents contours of total pressure at several axial locations along the intake, from the inlet to the outlet. The first slice shows the imposed inlet total pressure profile corresponding to a 30% incoming boundary-layer thickness. At the second slice, the optimizer has introduced a small bulge that extends from the top surface to the upper right and left sides and slightly raises the bottom wall. The third slice exhibits a dip in the middle of the top surface, resulting in two regions of low total pressure. The boundary layer also continues to thicken, leading to a larger region of low total pressure at the bottom surface. The dips observed on the left and right sides become more pronounced in the third slice, resulting in two small low-pressure regions that persist in the subsequent plane. At this stage, the bottom surface further flattens and the low total pressure flow gets pushed to the sides, increasing the circumferential uniformity of the flow towards the outlet and allowing the high total pressure region to remain centered at the exit plane. Figure 6 presents the outlet total pressure contours for the baseline duct (left) and the fully-converged multi-point optimized duct (right) operating with a 30% inlet boundary-layer height.

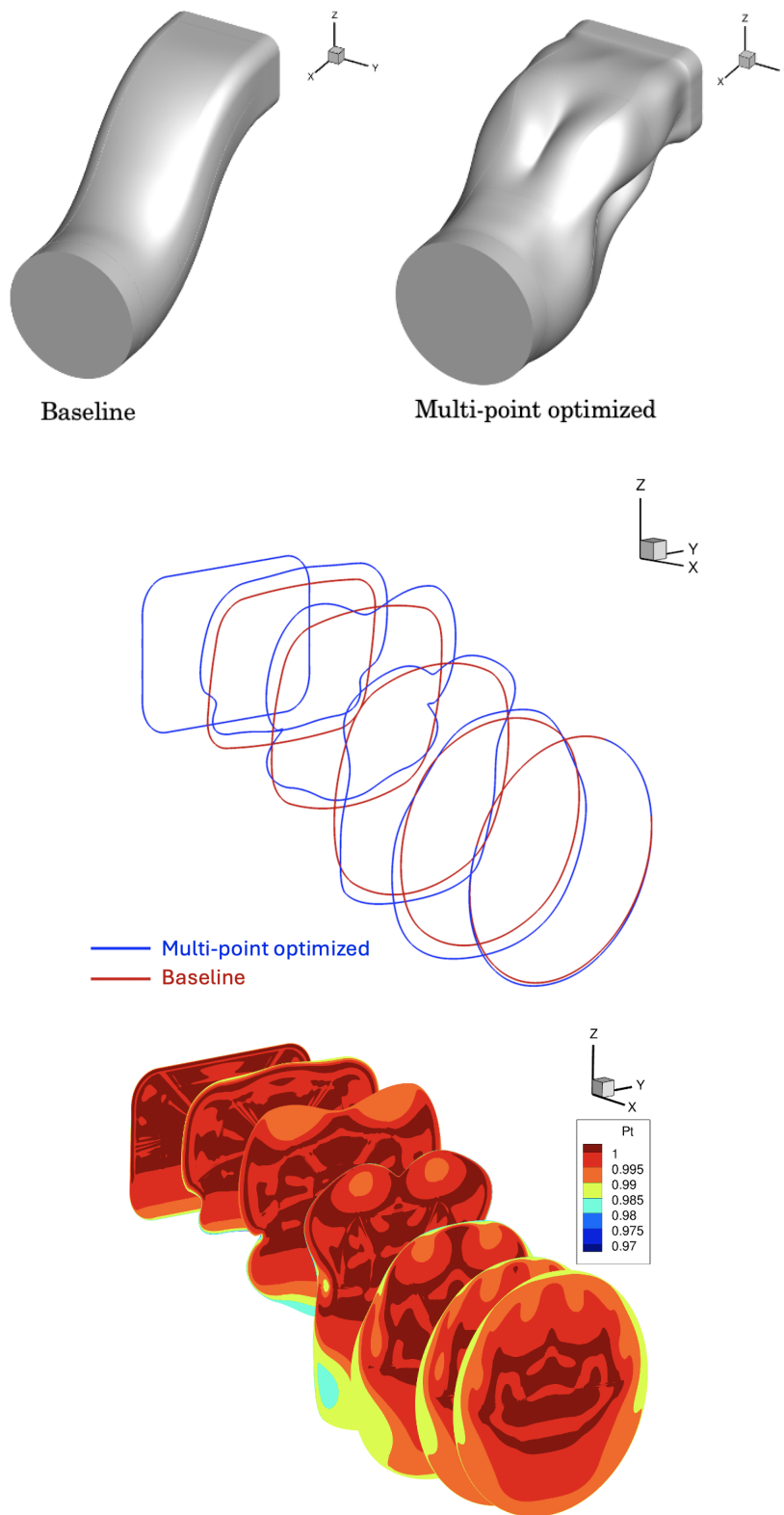


**Fig. 5** Comparison of the baseline and fully-converged multi-point optimized S-duct geometries (top and middle) and total pressure contours of the optimized duct (bottom)

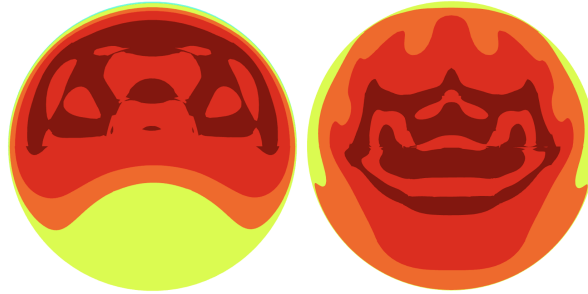


**Fig. 6 Comparison of outlet total pressure for the baseline (left) and fully-converged multi-point optimized S-duct at 30% boundary-layer height (right)**

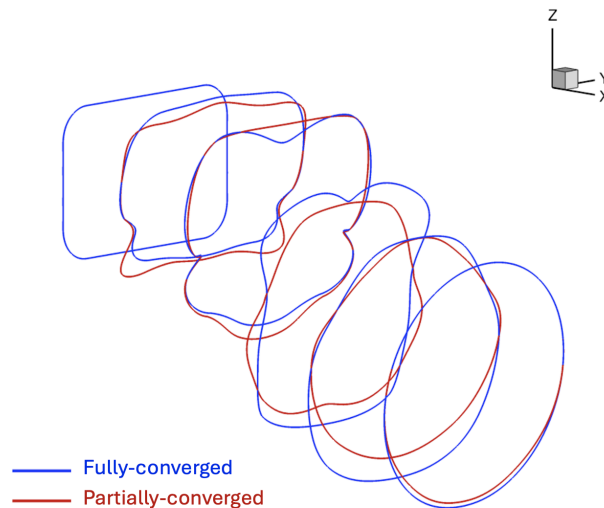


**Fig. 7 Comparison of the fully-converged and the partially-converged experimentally-validated multi-point optimized S-duct geometries**

## 2. Experimentally-Validated Case

Due to scheduling constraints associated with the testing facilities, the multi-point optimization case had not yet reached full convergence at the time the tests were scheduled to be conducted. Therefore, the partially converged configuration described below, which provides nearly equivalent performance to the fully-converged duct, was finalized and released for manufacturing and subsequent testing. A comparison of the converged and experimentally-validated multi-point optimized geometries is shown in Figure 7. For the 30% case, circumferential distortion of total pressure is reduced from the baseline duct value of  $41.9 \times 10^{-5}$  shown in Table 1 to  $1.35 \times 10^{-5}$  shown in Table 4, a reduction of roughly 97%. Although this value is slightly higher than the distortion value of  $1.25 \times 10^{-5}$  achieved by the fully-converged optimized duct shown in Table 3, it is nevertheless much lower than the baseline value. Therefore, experimental validation of the numerical predictions for this duct, as described in the next section, provides confirmation that the reductions in distortion predicted for the optimized duct can be reproduced experimentally.

## IV. Comparisons with Experiment

The partially-converged multi-point optimized S-duct presented above was manufactured and experimentally tested. Specifically, pressure distributions along the duct surface were measured experimentally, and comparisons were performed for the total pressure at the inlet and fan face, as well as for the integrated outlet quantities: total pressure recovery, circumferential total pressure distortion, and swirl.

**Table 4 Partially-converged experimentally-validated multi-point optimized performance values of pressure recovery, distortion, and swirl**

Objective	Multi-point (20%)	Multi-point (30%)	Multi-point (40%)
PR	0.99780	0.99774	0.99770
$D \times 10^5$	1.50	1.35	1.33
S	0.122	0.120	0.119

Figure 8 presents CFD predictions and experimental normalized total pressure contours at the outlet under different boundary-layer thicknesses at the inlet. Each row corresponds to increasing boundary-layer thickness, with CFD results on the left (a) and experimental data on the right (b). The CFD contours appear qualitatively aligned with the experimental results, with key trends well captured. In both cases, the high total pressure region at the center of the outlet shrinks as the boundary-layer thickness increases and the flow becomes more centered. This centralization effect is particularly visible in the experimental data. Although the outlet total pressure contours from the CFD and experiment are not identical, both display low circumferential distortion in comparison to that of the baseline duct shown in Figure 6.

Figure 9 compares the numerical and experimental inlet total pressure profile at 30% boundary-layer thickness and Mach number profiles for various boundary-layer thicknesses. The numerical results show good agreement with the experimental total pressure profile. However, the experimental Mach number curves show boundary-layer thicknesses that are larger than intended due to a static pressure gradient at the inlet caused by the bypass in the experimental setup. Similarly, for the numerical results, although the total pressure profile is as intended, and the mean Mach number outside the boundary layer is equal to the desired value, the Mach number profile is quite different from that seen in the experiment. These differences in the inflow Mach number profiles are partly responsible for the variations observed in the outlet total pressure profiles.

A comparison of numerical and experimental results for the performance metrics is presented in Figure 10. Pressure recovery shows good agreement with an incoming boundary-layer thickness of 30%. Circumferential distortion shows excellent agreement with incoming boundary-layer thicknesses of 20% and 30%, while the experimental distortion value is lower than the numerical one with a 40% incoming boundary-layer thickness. Overall, the experimentally-measured values of circumferential distortion confirm the ability of the optimization procedure to design an S-duct with low circumferential distortion. The experimental data generally show lower swirl magnitudes than the CFD predictions, probably due to the turbulence model used, as eddy viscosity models are known to be inaccurate for swirling flows [29]. Li and Liu [29] show that the quadratic constitutive relation (QCR) corrections improve accuracy in such flows but some error nevertheless can be expected. For total pressure and circumferential distortion, the discrepancies in the inlet Mach number profiles discussed above are likely to be the largest cause of the differences between computed and experimental results.

## V. Conclusions

A multi-point aerodynamic shape optimization was performed to design an S-duct intake for a boundary-layer-ingesting propulsion system using gradient-based optimization coupled with RANS flow simulations, and an optimized S-duct was fabricated and tested experimentally. The resulting S-duct geometry exhibited greatly reduced circumferential total pressure distortion at the fan face compared to the baseline unoptimized duct and less sensitivity to varying inflow conditions compared to a single-point optimized duct. Good to excellent agreement between CFD predictions and experimental measurements was observed in total pressure recovery, circumferential distortion, and swirl trends across all operating conditions. Most significantly, the experimental results show low circumferential distortion at the fan face, thereby confirming the ability of the optimization framework to make subtle geometric changes that lead to substantial reductions in distortion without sacrificing total pressure recovery.

## VI. Acknowledgements

The authors acknowledge the support of the National Research Council of Canada through the Low-Emissions Aviation Program and the NRC Aerospace Research Center. Computational resources were provided by the General Purpose Cluster supercomputer at the SciNet HPC Consortium.

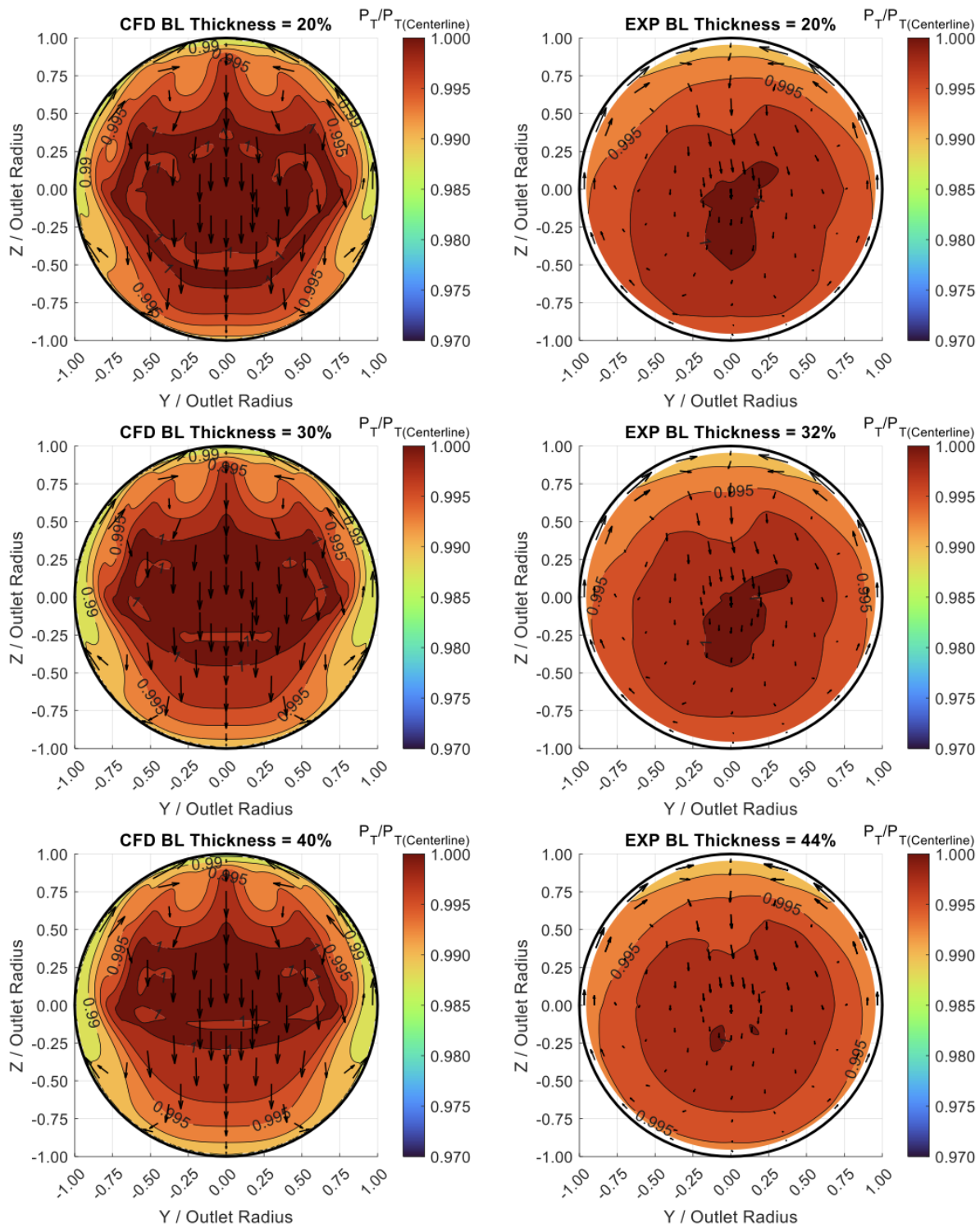
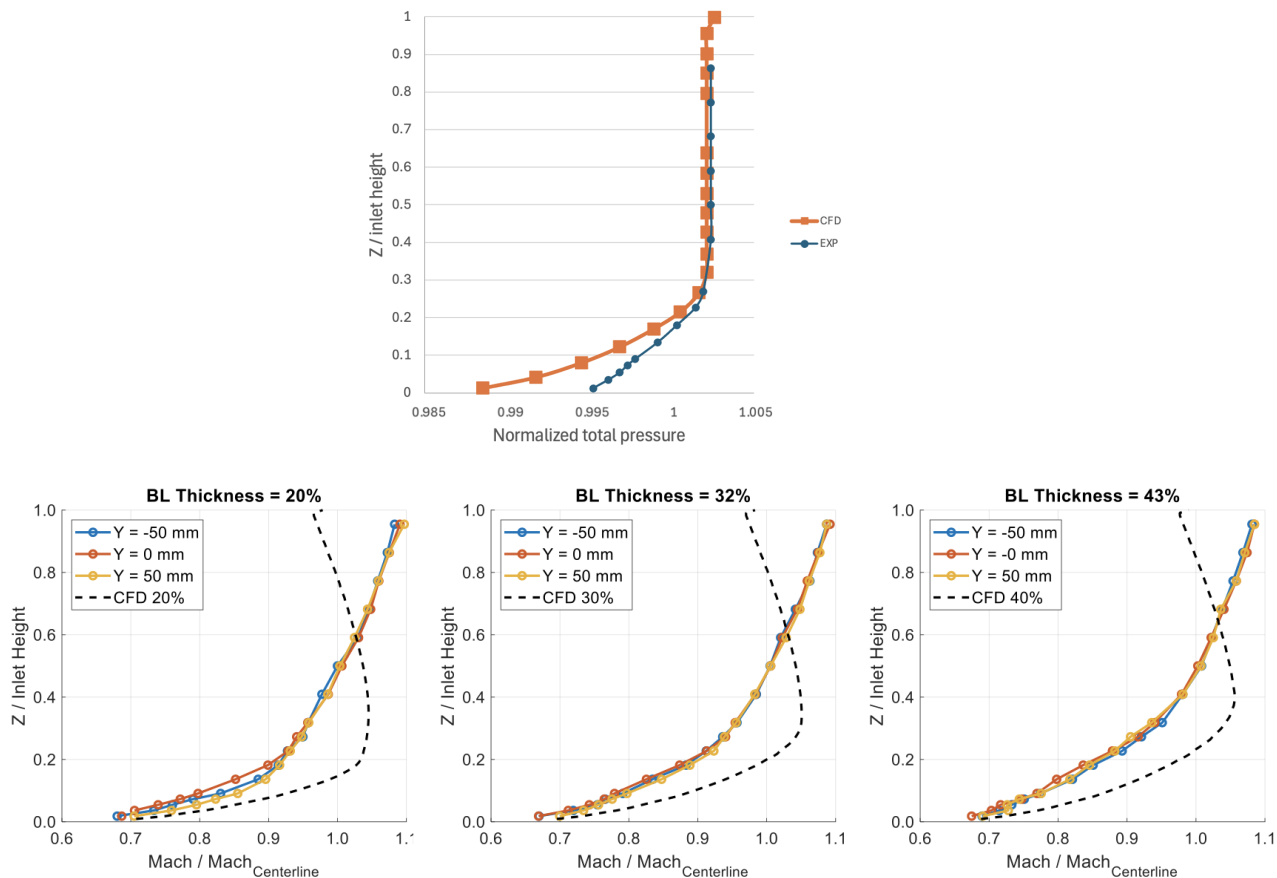
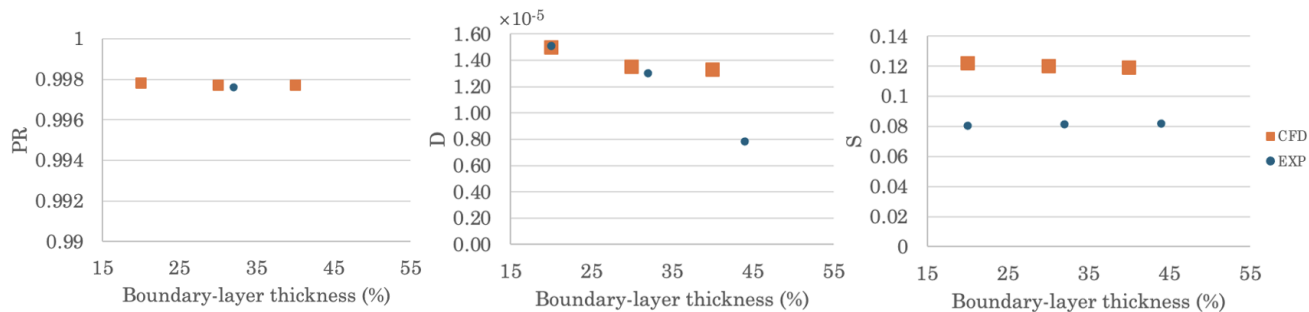


Fig. 8 Comparison of numerical and experimental outlet total pressure contours



**Fig. 9** Comparison of numerical and experimental inlet centerline total pressure profiles at 30% incoming boundary-layer thickness and inlet centerline Mach number profiles for various boundary-layer thicknesses



**Fig. 10** Comparison of numerical and experimental values of pressure recovery, circumferential distortion, and swirl for the partially-converged multi-point optimized duct

## References

- [1] Thurston, S., and Evanbar, M. S., "Efficiency of a Propulsor on a Body of Revolution-Inducing Boundary Layer Fluid," *Journal of Aircraft*, Vol. 3, No. 3, 1966, pp. 270–277. <https://doi.org/10.2514/3.43737>.
- [2] Brandau, J. H., "Performance of Waterjet Propulsion Systems: A Review of the State-of-the-Art," *Journal of Hydronautics*, Vol. 2, No. 2, 1968, pp. 61–73. <https://doi.org/10.2514/3.62775>.
- [3] Smith, L. H. J., "Wake Ingestion Propulsion Benefit," *Journal of Propulsion and Power*, Vol. 9, No. 1, 1993, pp. 74–82.
- [4] Hall, D. K., "Analysis of Civil Aircraft Propulsors with Boundary Layer Ingestion," Master's thesis, Massachusetts Institute of Technology, Cambridge, MA, 2004.
- [5] Gray, J. S., Mader, C. A., Kenway, G. K. W., and Martins, J. R. R. A., "Modeling Boundary Layer Ingestion Using a Coupled Aeropropulsive Analysis," *AIAA Journal*, Vol. 56, No. 1, 2017, pp. 1–12. <https://doi.org/10.2514/1.C034601>.
- [6] Kawai, R. T., Friedman, D. M., and Serrano, L., "Blended Wing Body (BWB) Boundary Layer Ingestion (BLI) Inlet Configuration and System Studies," Tech. Rep. NASA/CR-2006-214534, NASA, 2006.
- [7] Hall, D. K., Huang, A. C., Uranga, A., Greitzer, E. M., Drela, M., and Sato, S., "Boundary Layer Ingestion Benefit of the D8 Transport Aircraft," *AIAA Journal*, Vol. 55, No. 11, 2017, pp. 3693–3703. <https://doi.org/10.2514/1.J055755>.
- [8] Felder, J. L., Tong, M. T., Schnulo, S. L., Berton, J. J., Thacker, R. P., Haller, W. J., Kirk, J., and Guynn, M. D., "Updated Assessment of Turboelectric Boundary Layer Ingestion Propulsion Applied to a Single-Aisle Commercial Transport," NASA Technical Memorandum NASA/TM-20210016661, NASA Glenn Research Center, Cleveland, Ohio; NASA Langley Research Center, Hampton, Virginia, October 2022.
- [9] Berrier, B. L., and Morehouse, M. B., "Evaluation of Flush-Mounted, S-Duct Inlets With Large Amounts of Boundary Layer Ingestion," Symposium on Vehicle Propulsion Integration (Applied Vehicle Technology Panel Meeting), Warsaw, Poland, 6-9 Oct 2003, Paper No. 38 NASA/TP-2003-166030, NASA Langley Research Center, Hampton, Virginia, USA, 2003.
- [10] Zhang, Y., Yang, D., Dong, B., and Wang, S., "The Effect of Boundary-Layer Suction on the Performance of an Intake Under Off-Design Condition," *Journal of Applied Fluid Mechanics*, 2025.
- [11] Gartner, J., and Amitay, M., "Flow Control in a High-Offset Subsonic Air Intake," *47th AIAA/ASME/SAE/ASEE Joint Propulsion Conference Exhibit*, 2011. <https://doi.org/https://doi.org/10.2514/6.2011-5569>.
- [12] Wojewodka, M. M., White, C., Shahpar, S., and Kontis, K., "A Review of Flow Control Techniques and Optimisation in S-Shaped Ducts," *International Journal of Heat and Fluid Flow*, Vol. 74, 2018, pp. 223–235. <https://doi.org/10.1016/j.ijheatfluidflow.2018.06.016>.
- [13] Willmer, A., Brown, T., and Goldsmith, E., "Effects of Intake Geometry on Circular Pitot Intake Performance at Zero and Low Forward Speeds," *AGARD-CP-301*, 1981.
- [14] Zhang, W., Knight, D., and Smith, D., "Automated Design of a Three-Dimensional Subsonic Diffuser," *Journal of Propulsion and Power*, Vol. 16, No. 6, 2000, pp. 1132–1140. <https://doi.org/10.2514/2.5688>.
- [15] Koo, D., Zingg, D., Chishty, W., and Abo El Ella, H., "Optimizing Intakes for Embedded Engines," *24th ISABE Conference*, Canberra, Australia, 2019. ISABE-2019-24290.
- [16] Chiang, C., Koo, D., and Zingg, D. W., "Aerodynamic Shape Optimization of an S-Duct Intake for a Boundary-Layer Ingesting Engine," *Journal of Aircraft*, Vol. 59, No. 3, 2022, pp. 725–741. <https://doi.org/10.2514/1.C036632>.
- [17] Clark, C., Rasimarzabadi, F., Abo El Ella, H., Breton, H., Chikhaoui, I., and Zingg, D., "S-Duct with Boundary Layer Ingestion: Geometry Optimization and Validation," *AIAA SciTech Forum*, Orlando, FL, 2024. AIAA-2024-2331.
- [18] Papadopoulos, F., Valakos, I., and Nikolos, I., "Design of an S-duct intake for UAV applications," *Aircraft Engineering and Aerospace Technology*, Vol. 84, No. 6, 2012, pp. 439 – 456.
- [19] Gagnon, H., and Zingg, D. W., "Two-Level Free-Form and Axial Deformation for Exploratory Aerodynamic Shape Optimization," *AIAA Journal*, Vol. 53, No. 7, 2015, pp. 2015–2026. <https://doi.org/10.2514/1.J053575>.
- [20] Hicken, J. E., and Zingg, D. W., "Aerodynamic Optimization Algorithm with Integrated Geometry Parameterization and Mesh Movement," *AIAA Journal*, Vol. 48, No. 2, 2010, pp. 400–413. <https://doi.org/10.2514/1.44033>.

- [21] Osusky, M., and Zingg, D. W., "Parallel Newton-Krylov-Schur Flow Solver for the Navier-Stokes Equations Discretized Using Summation-By-Parts Operators," *AIAA Journal*, Vol. 51, No. 12, 2013, pp. 2833–2851. <https://doi.org/10.2514/1.J052487>.
- [22] Osusky, L., Buckley, H. P., Reist, T. A., and Zingg, D. W., "Drag Minimization Based on the Navier-Stokes Equations Using a Newton-Krylov Approach," *AIAA Journal*, Vol. 53, No. 6, 2015, pp. 1555–1577. <https://doi.org/10.2514/1.J053457>.
- [23] Asghar, A., Stowe, R. A., Allan, W. D. E., and Alexander, D., "Performance Evaluation of an S-Duct Diffuser of a Flight-Vehicle Inlet in High-Subsonic Flow," *ASME Turbo Expo 2015: Turbine Technical Conference and Exposition*, Montréal, Canada, 2015. <https://doi.org/10.1115/GT2015-43740>.
- [24] Yaras, M. I., and Grosvenor, A. D., "Evaluation of One- and Two-Equation Low-Re Turbulence Models. Part II - Vortex-Generator Jet and Diffusing S-Duct Flows," *International Journal for Numerical Methods in Fluids*, Vol. 42, No. 12, 2003, pp. 1321–1343. <https://doi.org/10.1002/flid.587>.
- [25] Gill, P. E., Murray, W., and Saunders, M. A., "SNOPT: An SQP Algorithm for Large-Scale Constrained Optimization," *SIAM Review*, Vol. 47, No. 1, 2005, pp. 99–131. <https://doi.org/10.1137/S0036144504446096>.
- [26] Roberts, J., and Walker, G., "Artificial Thickening of Wind Tunnel Boundary Layers via an Array of Cross-Flow Jets," *Experimental Thermal and Fluid Science*, Vol. 27, No. 5, 2003, pp. 583–588. [https://doi.org/10.1016/S0894-1777\(02\)00272-8](https://doi.org/10.1016/S0894-1777(02)00272-8).
- [27] Sargison, J., Walker, G., Bond, V., and Chavalier, G., "Experimental Review of Devices to Artificially Thicken Wind Tunnel Boundary Layers," *15th Australasian Fluid Mechanics Conference*, Sydney, Australia, 2004.
- [28] Pulliam, T. H., and Zingg, D. W., *Fundamental Algorithms in Computational Fluid Dynamics*, Springer, 2014.
- [29] Li, W., and Liu, Y., "Numerical Investigation of Corner Separation Flow Using Spalart–Allmaras Model with Various Modifications," *Aerospace Science and Technology*, Vol. 127, 2022, p. 107682. <https://doi.org/10.1016/j.ast.2022.107682>.